Thin Solid Films 520 (2012) 6709–6717

Contents lists available at SciVerse ScienceDirect

Thin Solid Films

journal homepage: www.elsevier.com/locate/tsf

Electrical properties of AlN_xO_y thin films prepared by reactive magnetron sputtering

J. Borges [a,*], N. Martin [b], N.P. Barradas [c], E. Alves [c], D. Eyidi [d], M.F. Beaufort [d], J.P. Riviere [d], F. Vaz [a], L. Marques [a]

[a] Centro de Física, Universidade do Minho, 4710-057 Braga, Portugal
[b] Institut FEMTO-ST, Département MN2S, UMR 6174 (CNRS, UFC, ENSMM, UTBM) 32, Avenue de l'Observatoire 25044 BESANCON Cedex, France
[c] Instituto Superior Técnico, Instituto Tecnológico Nuclear, E.N. 10, 2686-953 Sacavém, Portugal
[d] Institut PPRIME, UPR 3346 CNRS-Université de Poitiers-ENSMA, Département de Physique et Mécanique des Matériaux, BP 30179 86962 Chasseneuil-Futuroscope Cedex, France

ARTICLE INFO

Article history:
Received 19 January 2012
Received in revised form 15 June 2012
Accepted 24 June 2012
Available online 28 June 2012

Keywords:
Aluminum oxynitride
Magnetron sputtering
Electrical properties

ABSTRACT

Direct current magnetron sputtering was used to produce AlN_xO_y thin films, using an aluminum target, argon and a mixture of $N_2 + O_2$ (17:3) as reactive gases. The partial pressure of the reactive gas mixture was increased, maintaining the discharge current constant. Within the two identified regimes of the target (metallic and compound), four different tendencies for the deposition rate were found and a morphological evolution from columnar towards cauliflower-type, ending up as dense and featureless-type films. The structure was found to be Al-type (face centered cubic) and the structural characterization carried out by X-ray diffraction and transmission electron microscopy suggested the formation of an aluminum-based polycrystalline phase dispersed in an amorphous aluminum oxide/nitride (or oxynitride) matrix. This type of structure, composition, morphology and grain size, were found to be strongly correlated with the electrical response of the films, which showed a gradual transition between metallic-like responses towards semiconducting and even insulating-type behaviors. A group of films with high aluminum content revealed a sharp decrease of the temperature coefficient of resistance (TCR) as the concentration ratio of non-metallic/aluminum atomic ratio increased. Another group of samples, where the non-metallic content became more important, revealed a smooth transition between positive and negative values of TCR. In order to test whether the oxynitride films have a unique behavior or simply a transition between the typical responses of aluminum and of those of the correspondent nitride and oxide, the electrical properties of the ternary oxynitride system were compared with AlN_x and AlO_y systems, prepared in similar conditions.

1. Introduction

The research prompted by the industry, in order to develop a large variety of technologies, aims the production of materials that can perform different solicitations, where the electrical, mechanical, chemical, thermal and optical properties may be adjusted to configure a multifunctional behavior [1,2]. In this particular point, the magnetron sputtering is a very important technique capable of producing such materials [3] in the form of thin films, combining some attractive features and a significant number of possible property gradients. Two of the most relevant groups of materials used in coatings technology are the metal (Me) nitrides (MeN_x) and oxides (MeO_y), such as aluminum nitride, AlN, and aluminum oxide, Al_2O_3, whose properties are quite studied and its application widely spread in different technologies.

AlN is an excellent thermal conductor [4,5], with high stability and resistance to caustic chemical etching [6–8], being commonly used as substrate in several microelectronic devices. In one of its most common structural arrangements, it is a hexagonal (*wurtzite*) crystalline semiconductor with a large bandgap (~6.2 eV) [9,10], with very high electrical resistivity (~$10^{12}\Omega$.m) and high hardness [11]. Besides the *wurtzite* structure, AlN has also two cubic structures [10], where the electrical resistivity is even higher than that of hexagonal phase. Polycrystalline aluminum nitride has a high dielectric strength (4–5.5 $MV.cm^{-1}$) and a dielectric constant of ~9 (at 1 MHz), being used as a gate dielectric in high voltage and high power electronic devices. It is also a piezoelectric material [12] and it was considered a good alternative to zinc oxide (ZnO) in the last decade [13,14]. These specific properties allow the use of AlN material in the fabrication of optical sensors in the ultraviolet–visible region; light emitting diodes with one of the shortest emission wavelength reported (210 nm) [15]; high power and high temperature electronic devices; surface acoustic wave devices [16]; widely used as resonators and band-pass filters in communication systems; high-frequency (GHz) bulk acoustic wave devices

* Corresponding author at: Universidade do Minho, Departamento/Centro de Física, Campus de Gualtar, 4710-057, Braga, Portugal.
E-mail address: joelborges@fisica.uminho.pt (J. Borges).

0040-6090/$ – see front matter © 2012 Elsevier B.V. All rights reserved.
doi:10.1016/j.tsf.2012.06.062

[17]; film bulk acoustic resonator [18,19]; electronic packaging; among several other examples.

On the other hand, aluminum oxide (Al_2O_3) is one of the best corrosion protection materials, even at high temperatures [20], providing a protective barrier against both chemical corrosion and mechanical wear [21,22]. It is an insulator material that can exist in many metastable structures generally divided in two broad categories: face-centered-cubic (fcc) or hexagonal close packed arrangement of oxygen anions [23]. Alumina also reveals a high electrical breakdown field (5–30 $MV.cm^{-1}$), large bandgap (>9 eV), high permittivity (8.6–10) [24] and low refractive index [21]. Due to its dielectric properties, it has been considered a good replacement of SiO_2 in many electronic devices, such as flash memory circuits [25], organic thin film transistors [26], metal–oxide–semiconductor field-effect transistor [27], among others [28].

Aluminum oxynitride thin films (AlN_xO_y) have some interesting applications in different technological fields, such as protective coatings against wear, diffusion and corrosion, for oxidation resistance of epoxy films [29], as dielectric in multilayer capacitors with high energy density and wide temperature properties [4], among others [30]. However, the available knowledge on this particular system is still reduced [4,31–33] and the studies on the aluminum oxynitride are mainly related with its *spinel* structure [34–38].

The possibility to tailor the properties of the aluminum oxynitride films between pure aluminum to those of aluminum oxide and nitride films, or to combine some of their advantages by varying the concentration of aluminum, oxygen and nitrogen in the film, opens a significant number of possible applications for the Al–N–O system. One of such possibilities is within the electrical-driven applications. In fact, within the set of possible properties, an important feature of polycrystalline thin films is that their electrical resistivity (ρ) and its dependence on the temperature, can vary significantly in comparison with the correspondent bulk material (single-crystalline). This fact is closely related with the potential barriers and space charge regions created around grain boundaries [39,40] which will affect the charge carrier transport in the thin films.

Since the electrical properties of the materials significantly depend on their interdependence of composition and type of bonding, structure, and morphology, an understanding of these relationships will be a major concern in this work. For this purpose, a set of Al–N–O films was prepared by reactive magnetron sputtering and analyzed in terms of all the above items. This knowledge is fundamental to understand the electrical behavior of the material with increasing nitrogen/oxygen concentration, but also to establish the limits for practical applicability of these coatings in devices.

2. Experimental details

The thin films were deposited by reactive direct current (DC) magnetron sputtering in a home-made deposition system, mainly composed of a cylindrical deposition chamber (~40 dm^3), a vacuum system, a gas flow control system, an electrical system, a pre-chamber and a control unit. The deposition chamber is formed by four vertically rectangular magnetrons (unbalanced of type 2), in a closed field configuration. Only one magnetron was used to produce the films, powered by a Hüttinger PFG 7500DC (maximum output of 7.5 kW). The primary vacuum of the chamber (with pressures of ~0.3 Pa) is obtained by two parallel rotary vane vacuum pumps, a TRIVAC D 8B (pumping speed of 2.36 $L.s^{-1}$) and a Balzers Duo 012A (3.3 $L.s^{-1}$). The secondary vacuum (with pressures of ~10^{-4} Pa) is obtained using a Turbo Molecular high vacuum pump from Alcatel, model PTM 5400 (400 $L.s^{-1}$). In order to measure the gas pressure, the system is constituted by a Leybold Penningvac PTR225 (10^{-7}–10 Pa) and a Leybold Sky-Pirani Gauge TR090 (10^{-2}–10^5 Pa).

The films were prepared with the substrate holder positioned at 70 mm from the target in a rotation mode-type (9 rpm). The power supply connected to the magnetron was operated in current regulating mode by applying a DC current density of 75 $A.m^{-2}$ on the aluminum target (99.96% purity). The grounded substrates (glass and monocrystalline silicon wafers with (100) orientation) were heated before discharge ignition, by using a heating resistor, placed close to the surface of the substrate holder, controlled by a Type K thermocouple with the thermostat adjusted to 373 K. Before each deposition, the substrates were ultrasonically cleaned and then subjected to an *in situ* etching process in a pure argon atmosphere (pressure of 0.3 Pa, corresponding to a flow rate of 70 sccm), applying a pulsed DC current of 0.6 A (T_{on} = 1536 ns and f = 200 kHz) during 900 s.

For the preparation of the thin films, the aluminum target (200 × 100 × 6 mm^3) was sputtered using a gas atmosphere composed of argon (working gas, at the same 0.3 Pa partial pressure), and the reactive gas. In the case of the oxynitride films, AlN_xO_y, the reactive gas atmosphere was composed of a nitrogen + oxygen mixture, with a constant $N_2 + O_2$ ratio of 17:3 and flow rates of up to 10 sccm (corresponding to a partial pressure of 0.081 Pa). In the case of the binary systems, AlN_x and AlO_y films, the nitrogen (N_2) and oxygen (O_2) flow rates varied from 0 to 45 sccm (0 to 0.32 Pa) and from 0 to 9 sccm (0 to 0.07 Pa), respectively. The partial pressure of reactive gas was measured just before discharge ignition, without argon, and keeping constant the other deposition parameters (temperature, bias and base pressure of 1×10^{-3} Pa), and thus it is directly proportional to the gas flow rate. The total pressure is the sum of the partial pressure of argon (0.3 Pa), also measured prior to discharge ignition, with the partial pressure of the reactive gas used. A delay time of 5 min was used before positioning the surface of the samples in front of the Al target. This delay time was used to avoid film contamination resulting from previous target poisoning and also to assure a practically constant deposition temperature of the substrates during film growth.

The discharge parameters, namely target potential and current, gas pressure, argon flow and reactive gas flows, were monitored before and/or during the deposition using a Data Acquisition/Switch Unit Agilent 34970A with a multifunction module (334907A), where the cables (from analog outputs of the power supply, pressure sensors and flow controllers) were connected. This unit uses a RS-232 interface and the data is acquired with a *Benchlink Data Logger III* software.

The deposition rate, or growth rate, was calculated by the ratio between the average thickness of the sample, deposited on Silicon substrate, and the deposition time (2 h). Scanning electron microscopy (SEM) was used to determine the thickness of the films and to investigate their morphology, using a Leica Cambridge S360 apparatus.

The atomic composition of the as-deposited samples was measured by Rutherford Backscattering Spectrometry (RBS) using 1.4 and 1.75 MeV proton beams and a 2 MeV ^4He beam. Two different detectors were used at scattering angles of 140° and close to 180°, and experiments were made at tilt angles 0° and 30°. Composition profiles for the as-deposited samples were determined using the software NDF [41].

The structure and phase distribution of the coatings were accessed by X-ray diffraction (XRD), using a conventional Philips PW 1710 diffractometer, operating with Cu Kα radiation, in a Bragg–Brentano configuration. The XRD patterns were deconvoluted, assuming to be Pearson VII-type, to yield the peak position, peak intensity and integral breadth, using the *Winfit* software [42]. These parameters allowed calculating the interplanar distance, lattice parameters, preferential growth and grain size.

Transmission Electron Microscopy (TEM) observations were performed on a JEOL 2200-FS operating at 200 kV and equipped with a field-emission gun and an energy-filter (omega). Cross-sectional specimens were investigated in bright-field, dark-field, high-resolution and selected area diffraction modes.

The electrical resistivity of the films was determined using the four-point probe method (in linear geometry) [43] and in a Van der Pauw geometry [44,45]. For the high resistivity films, aluminum contacts (1 × 6 mm^2) were vapor-deposited on the top of the coating (in glass substrates), and the electrical resistivity of the films was obtained

from the I–V characteristics of the metal–insulator–semiconductor capacitor structure.

3. Results and discussion

3.1. Target potential and deposition rate

The evolution of the target potential, measured during the deposition of the films, is plotted in Fig. 1 as a function of the partial pressure of the reactive gas mixture (N_2+O_2) measured prior to discharge ignition. From the analysis of the results plotted in Fig. 1, one can notice that the equilibrium target potential values (estimated at steady state, when the voltage values were practically constant with deposition time) decrease almost linearly with the increase of the reactive gas partial pressure, varying from a maximum value of 452 V (film deposited without reactive gas) to a value of 320 V, correspondent to the preparation of a film with a reactive gas pressure of 5.4×10^{-2} Pa. For the films prepared with reactive gas pressures of 5.6×10^{-2} Pa, the target voltage abruptly drops to 267 V with no significant variation of the target potential thereafter, and thus the films prepared in this pressure window should be quite similar in terms of both chemical and physical properties.

Two major reasons explain the observed behavior of the target potential with increasing reactive gas partial pressure. On the one hand, the increase of reactive gas pressure in the chamber leads to a higher ionization probability (E_p), due to the rise of gas density. As a result, the minimum target potential (V_{min}) to sustain the discharge should decrease, since $V_{min.}\propto 1/E_p$. However, the increase of the reactive gas partial pressure induces also an increase of the ion implantation at the cathode surface, leading to a gradual increase of the ion induced secondary electron emission (γ_{ISEE}) coefficient of the Al target, contributing to the decrease of the cathode voltage ($V\propto 1/\gamma_{ISEE}$) [46–48]. For very high reactive gas pressures, an oxide compound layer is expected to be formed on the cathode surface. In this condition (target in a compound-like mode), the target becomes totally poisoned and the γ_{ISEE} coefficient of the target approaches to that of Al_2O_3, roughly two times higher than that of pure Al [49], which explains the sudden drop of target potential observed for a reactive gas partial pressure of 5.6×10^{-2} Pa.

An important feature of the produced films is illustrated in Fig. 2, where the values of the deposition rate, or growth rate since it is calculated by the average thickness per deposition time, are plotted as a function of the reactive gas partial pressure. Contrary to the simple two-fold variation of the target voltage (Fig. 1), the deposition rate

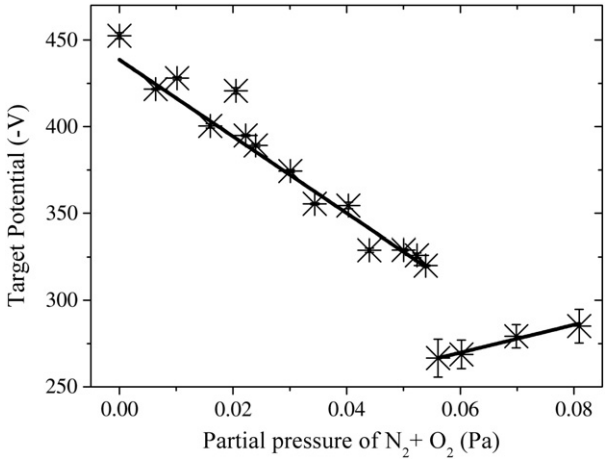

Fig. 1. Evolution of the target potential as a function of the partial pressure of reactive gas (N_2+O_2) in the chamber measured prior to discharge ignition. The error bars were estimated by the mean absolute deviation of the target potential values measured with the acquisition system. The total pressure is the sum of the argon partial pressure, measured prior to discharge ignition (0.3 Pa), with the partial pressure of reactive gas (x-axis value).

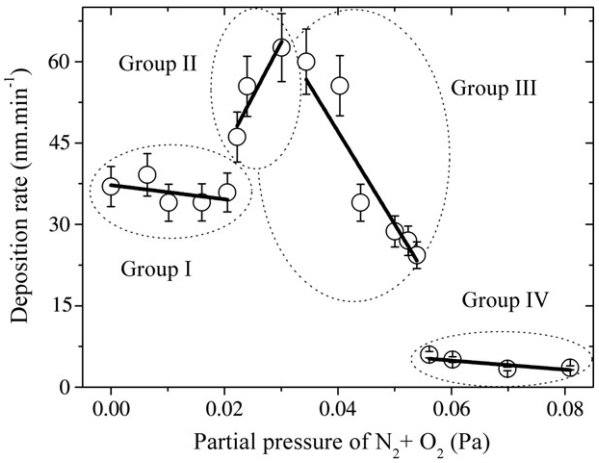

Fig. 2. Deposition rate of the AlN_xO_y samples as a function of the partial pressure of reactive gas. The error bars were estimated by maximum deviation to the average value.

plot, Fig. 2, is somewhat more complicated, revealing the possible existence of a wider number of different groups of samples. In fact, the first set of samples, for partial pressures up to 5.4×10^{-2} Pa, which revealed a steeply decrease of target potential (Fig. 1), shows now three distinct variation tendencies. The films prepared with reactive gas partial pressures up to 2.1×10^{-2} Pa have approximately constant values of the deposition rate, very close to 35 nm.min^{-1}. This first set of samples is then followed by a second group, where the deposition rate increase steeply up to about 63 nm.min^{-1} (corresponding to films prepared with gas mixture partial pressures varying from 2.2×10^{-2} Pa to about 3.0×10^{-2} Pa). Finally, a third set of samples can be identified, where the deposition rate starts to decrease continuously till a value close to 24 nm.min^{-1} (at 5.4×10^{-2} Pa). Interesting to note is that the previously mentioned second regime of the target potential values corresponds also to approximately constant values of deposition rate, around 5 nm.min^{-1}, between four and twelve times below those of the previous groups. Therefore, the films prepared with reactive gas pressures of 5.6×10^{-2} Pa and above, are most likely to have the target in a compound-like mode thus explaining the relatively low values of deposition rate. The samples of this last group probably have very similar behavior, contrary to those prepared with gas pressures below 5.6×10^{-2} Pa which are expected to have a gradient of responses. This means that the oxygen/nitrogen inclusion in the growing film might be important to tailor its properties between those of the Al/AlN_x and those of the correspondent oxide (AlO_y).

In general terms, the behavior of the deposition rate is closely related with the complex process of reactive magnetron sputtering, which depends on several parameters that are commonly strongly correlated. Indeed, the reactive gas used when preparing the films (a mixture of N_2 and O_2), not only reacts with the sputtered material from de aluminum target, but interacts also with the cathode surface, gradually covering it with a non-metallic compound layer, with a lower sputter yield than the initial metallic target [50,51]. According to Depla et al., the sputter yield can drop from a value of approximately 0.6 for the pure aluminum target towards 0.23 in the case of a compound target of aluminum oxide [52]. Since the amount of material that is deposited in the substrate per unit of time is correlated with the amount of atoms sputtered from the target, it could be expected to observe a general decrease of the deposition rate, due to increasing target coverage, as the reactive gas pressure increases, but that is not the case for the AlN_xO_y films. Furthermore, when the target becomes totally poisoned, it is expected that the deposition rate tends to constant values, as in fact observed in Fig. 2 for reactive gas partial pressures of 5.6×10^{-2} Pa and above.

In the case of the samples prepared with reactive gas pressures up to 2.1×10^{-2} Pa, the target stays almost clean (metallic mode) and thus the sputter yield is expected to be relatively high, which explains

the high deposition rates. Also, Fig. 2 shows that this group of samples (denoted as group I, Fig. 2) has approximately constant values of deposition rate, which might be explained by the compensation of the slight decrease of the sputtering rate expected with an increase in the incorporation of reactive gas atoms in the films. Regarding the second group of samples (referred as group II, Fig. 2), the evolution of the deposition rate may look unusual, since they are actually higher than those obtained for the films of the previous group. This fact can be understood by the analysis of the scanning electron microscopy, whose micrographs can be seen elsewhere [31]. Indeed, the type of growth of these films is significantly different. While the films indexed to group I have a typical columnar-like growth, the films of group II are porous with a cauliflower-like growth. Therefore, the high deposition rates within group II do not imply a higher quantity of material being deposited, but the formation of films with lower density. Further increase of the reactive gas partial pressure, group III of samples (Fig. 2), the deposition rate gradually decreases (also with a cauliflower-type of growth) as a direct consequence of the reduction of the target sputter yield. Finally, the group IV of samples (Fig. 2) is prepared with very low deposition rates since the target is most probably completely poisoned and the amount of metallic atoms sputtered is very low, thus explaining the roughly constant and low deposition rates within this zone. SEM analysis revealed, as expected, a dense, featureless-type of growth for these films.

3.2. Chemical composition

Fig. 3(a, b) shows the chemical composition results for the AlN_xO_y coatings obtained from RBS spectra analysis. The left side of the figure represents the variation of the atomic concentration of the different chemical elements (aluminum, nitrogen and oxygen), while in the right side it is plotted the concentration ratios of non-metallic over metallic elements of the AlN_xO_y films, both as a function of the partial pressure of the reactive gas mixture.

According to the results plotted in Fig. 3, one can argue that there are two different tendencies concerning the concentration of each chemical element in the film. The first one is observed for the films prepared with partial pressures of reactive gas mixture up to 5.4×10^{-2} Pa, and the second one for pressures of 5.6×10^{-2} Pa and above. Starting with aluminum content, its atomic concentration gradually decreases with the increase of the reactive gas pressure, from 100 at.% (roughly pure aluminum coating) to a value close to 54 at.% when the partial pressure of the reactive gas is 5.4×10^{-2} Pa, and then drops to 40 at.% for the film prepared with a reactive gas partial pressure of approximately 5.6×10^{-2} Pa. Concerning the nitrogen and oxygen content, it is clear from Fig. 3(a) that the incorporation of these elements is quite similar for partial pressures up to 5.4×10^{-2} Pa, where a gradual increase can be observed. Furthermore, comparing the atomic concentration of nitrogen and oxygen in each sample, the difference is always below 8 at.%, which is not very significant taking into account the uncertainty on the measurement (between 3 and 5 at.%). Although the reactive gas is composed of a mixture of N_2+O_2 with a fixed 17:3 ratio, the incorporation of these two non-metallic elements in each sample is not so different due to the well-known higher affinity of aluminum to oxygen, when compared to that for nitrogen. While the atomic content of oxygen varies from 0 to approximately 19 at.%, the nitrogen content reaches a maximum value of 27 at.%, for reactive gas partial pressures up to 5.4×10^{-2} Pa.

RBS results for the samples prepared with the highest reactive mixture partial pressures ($p_{N_2+O_2}\geq5.6\times10^{-2}$Pa) revealed that all the films have quite similar compositions, with an oxygen amount very close to 60 at.%, and an aluminum content of 40 at.%. Nitrogen concentration drops to residual values (non-detectable within the resolution of the experimental setup) in this set of films, reinforcing the higher affinity of aluminum to bond with oxygen, as demonstrated by the values of the Gibbs free energy of formation for aluminum oxide, $\Delta G^0_{f,@298K}(Al_2O_3)=-1.58\times10^6$J.mol^{-1} in comparison with that of the aluminum nitride, $\Delta G^0_{f,@298K}(AlN)=-2.87\times10^5$J.mol^{-1} [53]. The particular discharge conditions imposed by reactive gas mixture partial pressures of 5.6×10^{-2} Pa and above, induce a roughly stoichiometric composition of the films in the form of Al_2O_3 (alumina), with a concentration ratio (C_O/C_{Al}) of about 1.5. This fact can also be confirmed by the ternary phase diagram displayed in Fig. 4. As can be observed, the samples deposited with partial pressures of 5.6×10^{-2} Pa and above, are located in the close vicinity of the aluminum oxide compound. This group will be noted hereafter as the group C (compound-like films). Although the indexation of these samples was quite easy, the same cannot be claimed for the rest of the samples. In fact, this is somewhat difficult to ascertain from the concentration values, since the variation follows a roughly linear trend, as can be observed in Fig. 3(a). Nevertheless, if one follows the evolution of the concentration ratios, in particular C_{N+O}/C_{Al}, there are two different tendencies for reactive gas partial pressures up to 5.4×10^{-2} Pa. Fig. 3(b) shows that the increase of the incorporation of non-metallic elements is less pronounced within the group of films deposited with reactive gas partial pressures up to 3.0×10^{-2} Pa ($0.0<C_{N+O}/C_{Al}\leq0.18$), denoted hereafter as group M (metallic-like zone), if compared with the films deposited with reactive gas partial pressures above that value and below 5.4×10^{-2} Pa ($0.41<C_{N+O}/C_{Al}\leq0.85$), denoted hereafter as group T (transition zone). Moreover, the samples referred as the group M,

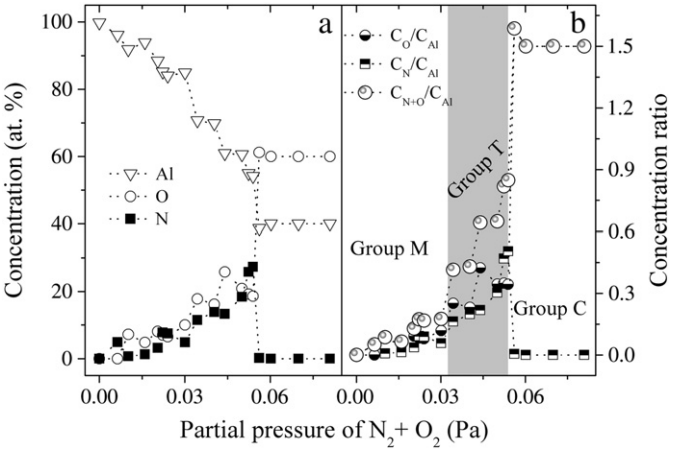

Fig. 3. Evolution of the (a) chemical composition in at.% and (b) concentration ratio, as a function of the partial pressure of reactive gas (N_2+O_2). The chemical composition of the samples was determined by RBS with an error of about 3–5 at.%.

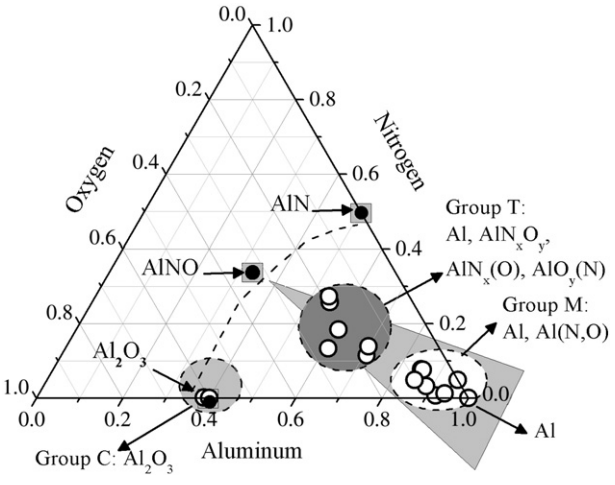

Fig. 4. Ternary phase diagram for the deposited AlN_xO_y films.

which encloses samples with different morphologies, *i.e.* groups I and II, reveal high metallic content, and an aluminum matrix with oxygen and nitrogen inclusions, Al (O, N), is expected to be formed. Furthermore, as a result of the low concentration ratio of non-metallic elements ($0<C_O/C_{Al}<0.12$ and $0<C_N/C_{Al}<0.09$), this group of samples has also a characteristic metallic-like color tone. In the case of group T films the incorporation of nitrogen and oxygen becomes much more pronounced, as can be observed in Fig. 3(b) by the jump of the concentration ratio from 0.18 ($p_{N_2+O_2}=3.0\times10^{-2}$Pa) to 0.41 ($p_{N_2+O_2}=3.4\times10^{-2}$Pa) from which the increase of the C_{N+O}/C_{Al} ratio is somewhat sharp, until a maximum value of 0.85 is reached for a pressure of 5.4×10^{-2} Pa. The oxygen and nitrogen concentration ratios also change more sharply in the previous group ($0.25\leq C_O/C_{Al}\leq0.42$ and $0.16\leq C_N/C_{Al}\leq0.50$). This set of results suggest the possibility to form sub-stoichiometric AlN_xO_y that can be sub-stoichiometric aluminum nitride doped with oxygen, $AlN_x(O)$, in some cases, and sub-stoichiometric aluminum oxide doped with nitrogen, $AlO_y(N)$, in others, as well as aluminum (doped) grains surrounded by aluminum oxide/nitride or oxynitride. The films within this zone T reveal dark-gray opaque surface tones, which is most likely the result of their decreasing metallic content. Another interesting feature that can be observed from the analysis of the ternary phase diagram (Fig. 4) is that the samples have chemical compositions somewhere inside a triangle where aluminum, aluminum nitride and aluminum oxide pure compounds are located in the vertices, supporting again the tendency to form AlN_xO_y compounds just before the transition to the stoichiometric Al_2O_3 films.

3.3. Structure of the films

The crystalline structure is an important characteristic of any given thin film system, which depends significantly on the particular composition of the films, but also on the basic deposition conditions, such as deposition rate, deposition temperature, gas pressures, *etc.* This fact can induce the production of films with a structure that can range from amorphous to polycrystalline (with different textures). Furthermore, the microstructure of the films is closely related with the size of the crystalline grains and their orientation, lattice defects, phase composition and also the surface morphology.

In order to study the structural features of the obtained films, a structural characterization was carried out. Fig. 5 shows XRD patterns for representative films prepared within the scope of the present work. From the analysis of the obtained results it is clear that the films prepared with reactive gas partial pressure below 5.4×10^{-2} Pa reveal crystalline-like structures, unlike the ones prepared with higher pressures that are amorphous. In a first approximation, these results are consistent with the previous analysis, exposing the correlation of the particular structural features with both composition and deposition parameters.

The pure aluminum film exhibits the characteristic fcc structure of (bulk) aluminum [54]. The two diffraction peaks revealed in Fig. 5 were identified for each sample, corresponding to the (111) and (200) planes of such fcc structure. The higher intensity of the (111) peaks is an indication of some preferential orientation of the grains. This preferred orientation is to be expected in a fcc structure since the coarsening of the grains during coalescence induces the growth of islands with the densest planes, the (111) in this particular case, as the microstructure of the film is evolving [55].

A second important feature is that in spite of the differences in the composition of the films and deposition conditions, the fcc structure is maintained for the films ascribed to groups M and T, ending up as a completely amorphous structure in the case of group C. Important to notice is also the evolution of the X-ray diffractograms for the samples of group T. In fact, showing some consistency with the changes observed in the morphology evolution and also in accordance with the changes analyzed in the deposition rate, the structure of these coatings is also gradually changing, revealing a clear tendency towards amorphization

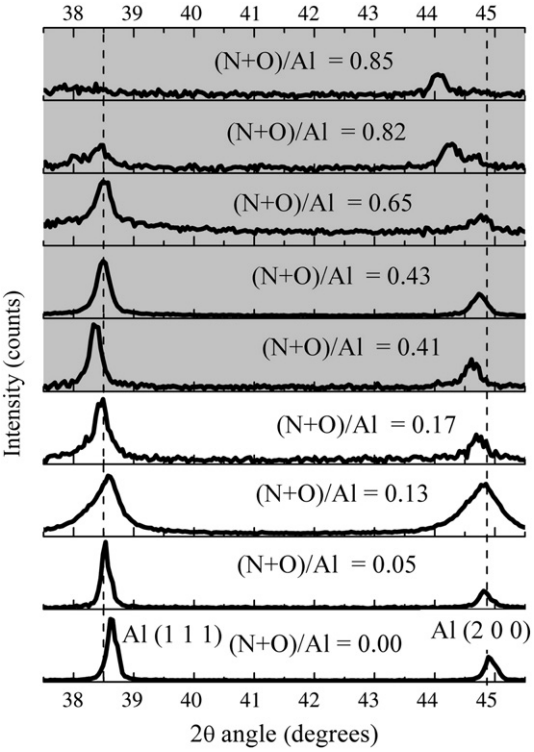

Fig. 5. X-ray diffraction patterns for the crystalline samples. The films indexed to group C (Al_2O_3) are amorphous.

as the non-metallic content increases. The overall changes in the group of samples indexed to group T are expected to give rise to a set of films with a relatively wide range of structural characteristics, mostly due to the increasing amounts of oxygen and nitrogen content, which are expected to induce defects such as interstitials, vacancies and some residual doping elements in the developed structures.

The values of the lattice parameter and grain size estimated by XRD peak fitting with a *Pearson VII* function, using the integral breadth method, were also evaluated. Concerning the lattice parameter, the deposited aluminum coating reveals a value of $a=0.403$ nm, which is slightly below the reference value of this material found in the available literature [56] ($a_{Al}=0.40496$ nm). Anyway, this is a typical behavior for the films produced by magnetron sputtering, denoting that the film must be in a compressive residual stress state [57]. Another important fact is that the lattice parameter of the polycrystalline films seems to have no significant variation (below 1%), although the concentration ratio of non-metallic over aluminum content of the films is gradually increasing. This could mean that aluminum matrix doping with oxygen and nitrogen is not occurring, and reinforcing the idea of the formation of amorphous AlN_xO_y matrix with Al grains.

The results of the grain size evaluation are plotted in Fig. 6. As it can be observed, there is a sharp decrease of this characteristic as a function of the concentration ratio (C_{N+O}/C_{Al}), varying from 52 nm (for the "pure" Al film, $C_{N+O}/C_{Al}=0.0$) to 14 nm (for the film with an atomic ratio C_{N+O}/C_{Al} of 0.13), corresponding to a decrease higher than 70%. This tendency can be explained by the incorporation of oxygen in the films that is segregated to the surface and grain boundaries, which inhibits the grain coarsening during coalescence and film growth due to the reduced mobility of aluminum atoms on oxide layers [55]. Interesting to note is the behavior that can be observed for the grain size evolution when the type of growth evolves from columnar to cauliflower-type, revealing a straight correlation between the structural and morphological growth. Indeed, within the group M, the grain size evaluation shows an inflection as the non-metallic over aluminum content increases, reaching a value of about 32 nm (for the film prepared with an atomic ratio C_{N+O}/C_{Al} of

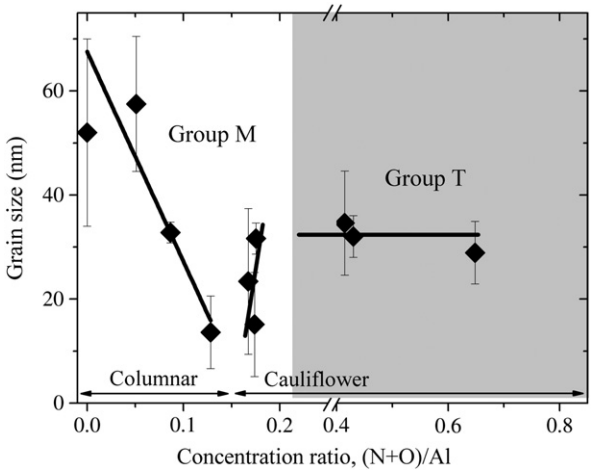

Fig. 6. Grain size of the face centered cubic crystals (Al-type structure) as a function of the non-metallic over aluminum atomic ratio. The error bar was estimated from the reliability of the fit (*winfit* software).

0.18). This behavior is consistent with the formation of round shape grains, whose growth is completely blocked by a surrounding oxide layer in an early stage of grain formation [55]. The grain size of the samples within the group T is barely the same (around 30 nm for C_{N+O}/C_{Al} atomic ratios varying from 0.41 to 0.65), except for the higher concentration ratios, where the samples are found to be quasi-amorphous.

Concerning the films indexed to the group C, where the concentration ratio of oxygen/aluminum is close to the stoichiometric condition, *i.e.* 1.5, the films are amorphous. This is in fact an expected result since the deposition temperature is low compared to the minimum temperature required to the synthesis of crystalline alumina [55,58].

3.4. Electrical properties

A close correlation of the electrical properties with the structure and composition of the films was observed. Fig. 7(a) shows the electrical resistivity (ρ) of the AlN_xO_y films, measured at room temperature, as a function of the concentration ratio of non-metallic/metallic elements (C_{N+O}/C_{Al}). From the analysis of Fig. 7(a), one can distinguish three different zones of evolution of the electrical resistivity, which is gradually changing from low values towards very high values, as the non-metallic content of the films increases.

The first zone corresponds to the group M of samples, with low ρ values, exhibiting electrical resistivity characteristic of metallic-like materials. The pure aluminum film reveals an electrical resistivity of about 3×10^{-8} Ω.m, using both measurement methods (four point probe in line and Van der Pauw geometry), very close to the common values claimed in the literature for aluminum bulk resistivity [59]. The electrical resistivity of the films then increases about two orders of magnitude towards a value of about 5.6×10^{-6} Ω.m, as the concentration ratio raises to 0.18. A second zone follows (corresponding to group T films), with the electrical resistivity increasing slightly from a value of 9.7×10^{-6} Ω.m to a value of 1.2×10^{-4} Ω.m, for concentration ratios between 0.41 and 0.85, respectively. These high values of resistivity are to be expected due to high non-metallic content of the films and also to the high porosity morphology revealed by these coatings [31], which constitutes a barrier to the flow of the electrical current.

Finally, the group C of samples (alumina-like coatings) exhibits very high values of electrical resistivity, varying between 10^{11} and 10^{12} Ω.m, in agreement with the values found in the literature for aluminum oxide thin films [24,25].

In order to study whether the oxynitride films have a unique behavior or are simply a transition between the typical responses of aluminum and of those of the correspondent nitride and oxide, two sets of the

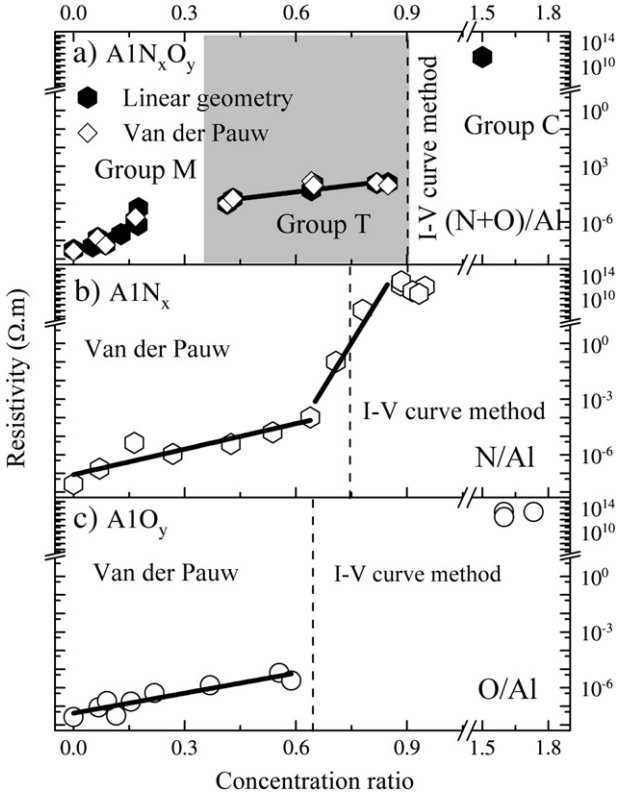

Fig. 7. Electrical resistivity, measured at room temperature, of the (a) AlN_xO_y, (b) AlN_x and (c) AlO_y systems, as a function of the non-metallic over aluminum atomic ratios.

binary systems, AlN_x and AlO_y, were also prepared and characterized in detail in terms of their electrical responses. In both binary systems, the electrical resistivity reveals the same tendency for an increase with the increase of the concentration ratio of the non-metallic over aluminum contents. Fig. 7(b) shows the evolution of the electrical resistivity of the AlN_x system as a function of C_N/C_{Al}. As it can be observed, the electrical resistivity gradually increases from 3×10^{-8} Ω.m to 1×10^{-4} Ω.m, as the concentration ratio of non-metallic elements, C_N/C_{Al}, increases from 0 to 0.64. For a concentration ratio of 0.71 the electrical resistivity sudden jumps several orders of magnitude reaching a value of 1×10^{-1} Ω.m. For even higher concentration ratios 0.88–0.95 (*quasi* stoichiometric films), the films revealed a very high electrical resistivity of about $10^{11}/10^{12}$ Ω.m, typical of an insulator material such as aluminum nitride [8]. Concerning the AlO_y films, the electrical resistivity as a function of the C_O/C_{Al} atomic ratio is plotted in Fig. 7(c). This figures shows that there is a very abrupt transition between the conducting films towards the insulator ones. The conducting films have a smooth variation of electrical resistivity of about two orders of magnitude, changing from 3×10^{-8} Ω.m to 3×10^{-6} Ω.m with the concentration ratio (C_O/C_{Al}) varying from 0.0 to 0.59. For a concentration ratio of $C_O/C_{Al}=1.6$, a sudden jump of twelve orders of magnitude is then observed, to a value of resistivity of $10^{12}/10^{13}$ Ω.m, being a direct consequence of the formation of roughly stoichiometric alumina-like films.

To better understand the conduction mechanisms of the films, the electrical resistivity was also measured as a function of the temperature, using the four point probe technique, in a Van de Pauw geometry [44,45]. Fig. 8(a) shows the evolution of the electrical resistivity of the AlN_xO_y films as a function of temperature. As it can be observed, there are two major types of films. For concentration ratios up to 0.43, the electrical resistivity increases as a function of the temperature. For higher concentration ratios (between 0.65 and 0.85), the electrical resistivity decreases as the temperature raises. The temperature coefficient of resistance [60] (TCR) values of the AlN_xO_y films, calculated at

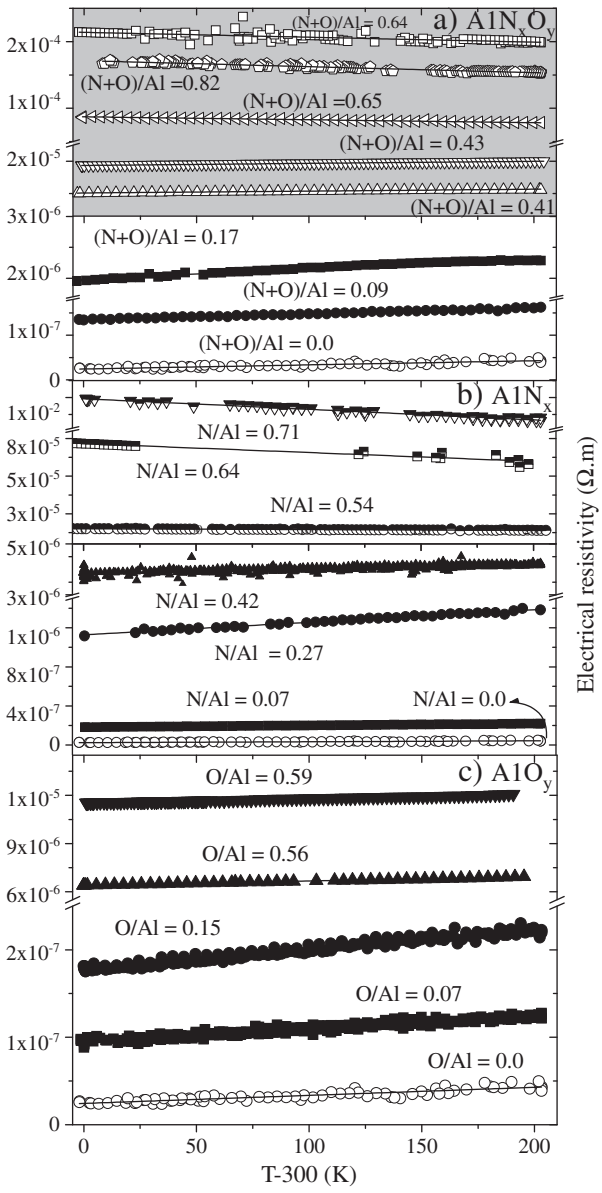

Fig. 8. Electrical resistivity evolution of the (a) AlN_xO_y, (b) AlN_x and (c) AlO_y films as a function of the temperature.

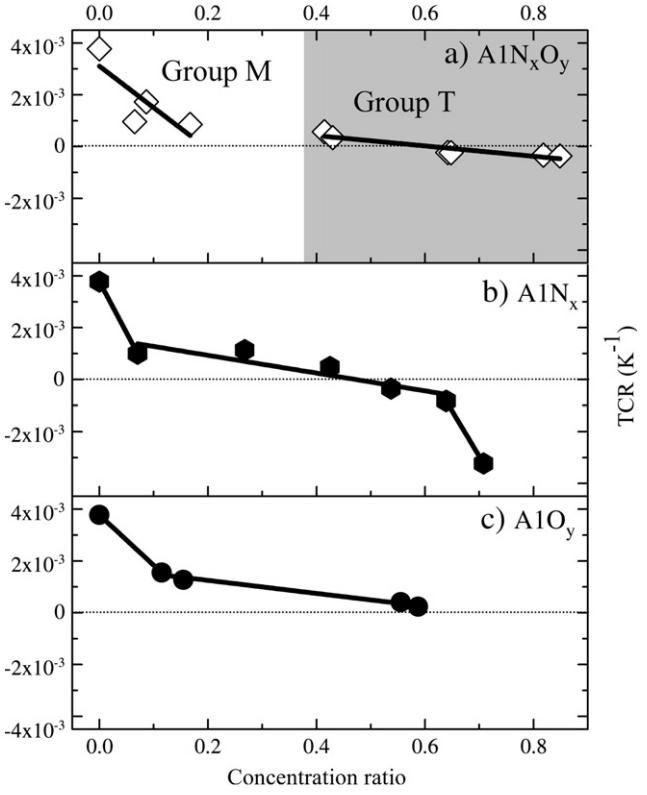

Fig. 9. Temperature coefficient of resistance, calculated at 300 K, of the (a) AlN_xO_y, (b) AlN_x and (c) AlO_y films as a function of the non-metallic over aluminum atomic ratio.

300 K, are plotted in Fig. 9(a). The aluminum coating has a TCR value of 4×10^{-3} K^{-1}, very close to the TCR of bulk aluminum (4.4×10^{-3} K^{-1}) found in the literature [61]. As the concentration ratio of non-metallic over aluminum elements increases, the TCR value is reduced to a value of about 8.5×10^{-4} K^{-1}, for concentration ratios up to 0.18, which includes the films indexed to group M. Concerning the group T of samples, where the content of non-metallic elements over aluminum is more important and a gradual amorphization of the films is observed, one can report a smoother decrease of TCR values compared to the group M. Nevertheless, an inversion of the slopes of the electrical resistivity *versus* temperature can be also reported, Fig. 8(a). Indeed, the TCR for the film with concentration ratio of 0.41 is 5.7×10^{-4} K^{-1} and the film with C_{N+O}/C_{Al} of 0.64 has actually a negative TCR, with a value of -2.3×10^{-4} K^{-1}. Furthermore, the TCR reaches a minimum value of -3.6×10^{-4} K^{-1} for a ratio of 0.85. This means that for ratios between 0.64 and 0.85 the resistivity decreases with increasing temperature, as shown in Fig. 8(a).

Concerning the electrical behavior of the AlN_x system, it is clear from Fig. 8(b) the existence of two groups of films for concentration ratios up to $C_N/C_{Al}=0.71$, corresponding to the lower values of electrical resistivity. One group stands for samples with atomic ratios up to 0.42, where the resistivity *versus* temperature slope is positive and another one for ratios between 0.54 and 0.71, where the slope becomes negative. When the atomic ratio is $C_N/C_{Al}\geq0.78$, the electrical resistivity is too high to be measured by the Van der Pauw technique. The TCR for the correspondent films are plotted in Fig. 9(b). As it can be observed, the TCR drops ~75%, from 4.0×10^{-3} K^{-1} ($C_N/C_{Al}=0$) to a value close to 1.0×10^{-3} K^{-1}, for an atomic ratio C_N/C_{Al} of 0.07. Then, a smooth decrease is observed between the atomic ratios (C_N/C_{Al}) of 0.27 and 0.64. The value of TCR becomes actually negative (-3.5×10^{-4} K^{-1}) when concentration of nitrogen/aluminum reaches 0.54. Finally a significant jump to -3.0×10^{-3} K^{-1} can be observed when the atomic ratio C_N/C_{Al} is 0.71.

In the case of the AlO_y system, the slope of resistivity *versus* temperature is positive for concentration ratios up to $C_O/C_{Al}=0.59$, which is consistent with the metallic behavior of these films, Fig. 8(c). The corresponding TCR value of these films is plotted in Fig. 9(c) as a function of the atomic ratio (C_O/C_{Al}). When the atomic ratio C_O/C_{Al} in the film increases to 0.11, the TCR value drops about 60% to a value of 1.6×10^{-3} K^{-1}, decreasing then slightly until a minimum value of 2.4×10^{-4} K^{-1} is reached for the film with atomic concentration ratio C_O/C_{Al} of 0.59.

Based on the results plotted in Figs. 8(a–c) and 9(a–c), it is obvious that the AlN_xO_y system has a different electrical response when compared with the binary systems, AlN_x and AlO_y, and thus opening the possibility to tailor its properties according to the particular application envisaged.

According to the previous discussion, it is clear that the electrical resistivity and the TCR evolution of the three systems of films strongly depend on the chemical composition of the films. As the concentration of non-metallic atoms increases, the electrical resistivity (at room temperature) suffers a large variation from low values, typical of aluminum metal, towards very high values, characteristic of insulators. In what

concerns the TCR of the films, it changes from a positive value for metallic films decreasing progressively towards values close to zero (AlO_y) or negative values (AlN_xO_y and AlN_x), as the concentration ratio increases.

This variation of the electrical properties with non-metallic over metallic atomic ratios can be easily explained assuming that the electrical transport in the film takes place through a series of channels formed by metallic grains. Some of the grains in a channel can be in contact, and, in this case, the current conduction is governed by the constrictions between grains. However other grains are separated by a thin insulating barrier, forming metal–insulator–metal (MIM) units, and, in this case, the electrical transport is controlled by tunneling processes, such as thermally activated tunneling and/or tunneling through localized states in the insulating layer [62,63]. For N parallel channels, each consisting of N_C resistors of the conducting type R_C, and N_B MIM units with barrier resistance R_B, the total resistance of this network of resistors may be written as [62]:

$$R(T) = R_C(T) + R_B(T) = N_C R_{C,0}\frac{[1+\alpha_C(T-T_0)]}{N^2} + \frac{N_B}{2N^2}R_{B,0}\frac{\sin bT}{bT}[1+exp(E/kT)] \quad (1)$$

where $R_{C,0}$ is the constriction resistance at the reference temperature T_0, α_C the TCR of the conducting component at the reference temperature T_0, $R_{B,0}$ and b are factors depending on barrier parameters (height and thickness), and E is the activation energy for thermally activated tunneling. In the case of the deposited films, when the concentration ratio C_{N+O}/C_{Al} in the films increases, both components of the total resistance also increase. The barrier resistance (R_B) raises due to the formation of the insulating aluminum oxide/nitride or oxynitride amorphous matrix surrounding aluminum grains (Fig. 10, TEM image), and thus the barrier thickness in MIM structures is large. The growth of the oxide/nitride (or oxynitride) matrix leads also to limitation of aluminum grain size, which leads to a larger electron scattering at grain boundaries and thus to an increase in importance of the conducting component (R_C). This can explain the increase of film resistivity observed previously as a function of the non-metallic over aluminum atomic ratios, in AlN_xO_y, AlN_x and AlO_y systems.

The temperature coefficient of resistance of the structure is the superposition of the TCR of the conducting (α_C) and barrier components (α_B):

$$\frac{dR}{dT}\frac{1}{R} = \beta\alpha_B + (1-\beta)\alpha_C \quad (2)$$

where $\beta = \frac{R_B}{R_C+R_B}$ is the fractional barrier resistance. The TCR of the conducting component (α_C) is positive, while the TCR of the barrier component is negative and given by:

$$\alpha_B = \frac{1}{R_B}\frac{dR_B}{dT} = b\cot(bT) - \frac{1}{T} - \frac{E}{kT^2}[1+exp(-E/kT)] \quad (3)$$

When the non-metallic over metallic atomic ratio in the films increases, the fractional barrier resistance, β, tends to increase due to the larger barrier resistance. On the other hand, the increase of the scattering component of the constriction resistance, due to the limitation of the grain size, contributes to the reduction of the TCR of this component, α_C. Due to both effects the barrier component may become dominant in TCR, Eq. (2), thus explaining the negative TCR of some films for large C_{N+O}/C_{Al} ratio.

4. Conclusions

AlN_xO_y thin films were deposited by reactive DC magnetron sputtering, using an aluminum target. Argon was used as working gas and a mixture of nitrogen and oxygen as reactive gases (17:3 ratio). The target potential, deposition rate, chemical composition, structure and morphology of the films were correlated with the partial pressure of reactive gas injected in the chamber. Increasing the partial pressure of reactive gas allowed the production of AlN_xO_y films with different features concerning its chemical composition, structure, morphology and electrical responses. The target potential decreased gradually, until an approximately constant value was reached (compound-like mode). The morphology of the films gradually evolves from a typical columnar-like growth towards a cauliflower-type, ending up as dense and featureless-like structure, for high pressures of reactive gas. As a consequence of the target condition and pressure in the chamber, the deposition rate was constant for low pressures. Then, it increased as the morphology changed to cauliflower-type, decreasing again, maintaining the same type of growth. Finally, one can report that the deposition rate remained approximately constant in the case of the dense films, deposited with the target in compound-like mode. According to the chemical analysis it was possible to categorize the samples in three different groups, concerning their particular atomic ratio values. The structure of the films was found to be of aluminum-type (face centered cubic) and it was maintained in the first two groups identified, with a gradual amorphization especially in the alumina-like group.

The electrical resistivity measurements revealed different electrical responses, according to the particular atomic ratio values in the films. The electrical resistivity, measured at room temperature, increased

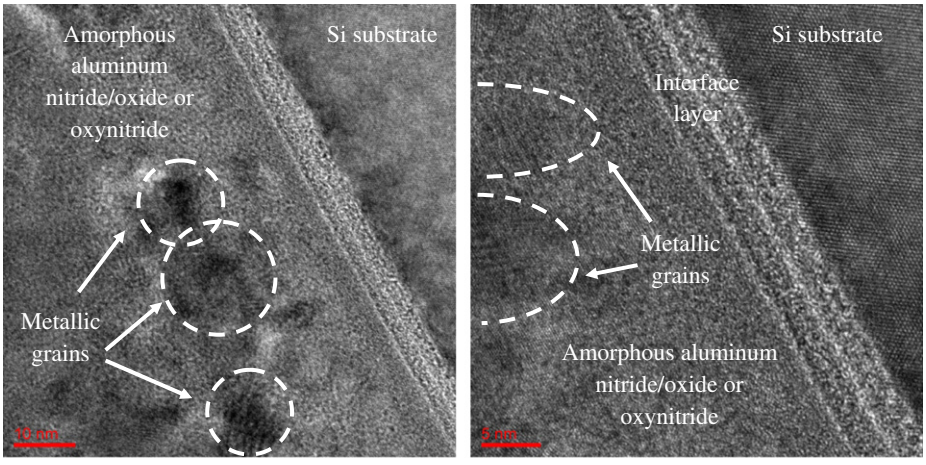

Fig. 10. High-resolution transmission electron microscopy showing that the films must be composed of amorphous aluminum nitride/oxide or oxynitride surrounding metallic (aluminum) grains.

rapidly in the samples from groups M and T. The calculation of the temperature coefficient of resistance revealed that there is a transition behavior in group T of samples, where the TCR values evolute from positive to negative ones. The stoichiometric alumina films, group C, were confirmed to be electrical insulators. The variation of the electrical properties with non-metallic over metallic atomic ratios was explained assuming that the electrical transport in the film takes place through a series of channels formed by aluminum grains separated by thin insulating barriers, forming metal–insulator–metal (MIM) units. The increase of film resistivity observed as a function of the non-metallic over aluminum atomic ratios, in AlN_xO_y, AlN_x, AlO_y systems can be explained by growth of the oxide/nitride (or oxynitride) matrix leading to a larger electron scattering at grain boundaries, due to the limitation of aluminum grain size, and to an increase of the barrier thickness in MIM structures. Simultaneously, the barrier component of resistance, which has a negative dependence on temperature, becomes dominant thus explaining the negative TCR of the films for large C_{N+O}/C_{Al} non-metallic over aluminum atomic ratios.

Acknowledgments

This research is sponsored by FEDER funds through the program COMPETE-Programa Operacional Factores de Competitividade, by the national funds through FCT-Fundação para a Ciência e a Tecnologia, under the project PTDC/CTM-NAN/112574/2009 and Programa Pessoa 2010/2011 Cooperação Portugal/França, Proc.º 441.00, Project"*COLOURCLUSTER*". J. Borges is grateful to Maxime Vallet, from University of Poitiers, for his help in preparing samples for TEM analysis. J. Borges also acknowledges FCT financial support under PhD grant no. SFRH/BD/47118/2008.

References

[1] P. Carvalho, F. Vaz, L. Rebouta, L. Cunha, C.J. Tavares, C. Moura, E. Alves, A. Cavaleiro, P. Goudeau, E. Le Bourhis, J.P. Riviere, J.F. Pierson, O. Banakh, J. Appl. Phys. 98 (2) (2005) 023715.
[2] P. Carvalho, J.M. Chappe, L. Cunha, S. Lanceros-Mendez, P. Alpuim, F. Vaz, E. Alves, C. Rousselot, J.P. Espinos, A.R. Gonzalez-Elipe, J. Appl. Phys. 103 (10) (2008) 104907.
[3] P.J. Kelly, R.D. Arnell, Vacuum 56 (3) (2000) 159.
[4] K.R. Bray, R.L.C. Wu, S. Fries-Carr, J. Weimer, Thin Solid Films 518 (1) (2009) 366.
[5] Q. Xia, H. Xia, A.L. Ruoff, J. Appl. Phys. 73 (12) (1993) 8198.
[6] Z. An, C. Men, Z. Xu, P.K. Chu, C. Lin, Surf. Coat. Technol. 196 (1–3) (2005) 130.
[7] N. Rakov, A. Mahmood, M. Xiao, Scr. Mater. 50 (5) (2004) 589.
[8] H.C. Barshilia, B. Deepthi, K.S. Rajam, Thin Solid Films 516 (12) (2008) 4168.
[9] R.D. Vispute, J. Narayan, J.D. Budai, Thin Solid Films 299 (1–2) (1997) 94.
[10] J. Wang, W.L. Wang, P.D. Ding, Y.X. Yang, L. Fang, J. Esteve, M.C. Polo, G. Sanchez, Diam. Relat. Mater. 8 (7) (1999) 1342.
[11] L. Yate, J.C. Caicedo, A.H. Macias, F.J. Espinoza-Beltran, G. Zambrano, J. Munoz-Saldana, P. Prieto, Surf. Coat. Technol. 203 (13) (2009) 1904.
[12] V. Mortet, M. Nesladek, K. Haenen, A. Morel, M. D'Olieslaeger, M. Vanecek, Diam. Relat. Mater. 13 (4–8) (2004) 1120.
[13] D. Marc-Alexandre, M. Paul, Appl. Phys. Lett. 74 (20) (1999) 3032.
[14] F. Martin, P. Muralt, M.A. Dubois, A. Pezous, J. Vac. Sci. Technol., A 22/2 (2004) 361.
[15] Y. Taniyasu, M. Kasu, T. Makimoto, Nature 441 (7091) (2006) 325.
[16] Q.X. Guo, M. Yoshitugu, T. Tanaka, M. Nishio, H. Ogawa, Thin Solid Films 483 (1–2) (2005) 16.
[17] J. Xiong, H.-S. Gu, K. Hu, M.-Z. Hu, Int. J. Miner. Metall. Mater. 17/1 (2010) 98.
[18] W.-J. Liu, S.-J. Wu, C.-M. Chen, Y.-C. Lai, C.-H. Chuang, J. Cryst. Growth 276 (3–4) (2005) 525.
[19] K. Li, H. Jin, D.-M. Wang, Y.-F. Tang, J. Zhejiang Univ. Sci. A 10/3 (2009) 464.
[20] A. Aryasomayajula, S. Canovic, D. Bhat, M.H. Gordon, M. Halvarsson, Thin Solid Films 516 (2–4) (2007) 397.
[21] H. Demiryont, L.R. Thompson, G.J. Collins, J. Appl. Phys. 59 (9) (1986) 3235.
[22] J.M. Schneider, W.D. Sproul, A. Matthews, Surf. Coat. Technol. 98 (1–3) (1998) 1473.
[23] L. Igor, B. David, J. Am. Ceram. Soc. 81 (8) (1998) 1995.
[24] R.K. Bhan, A. Jain, D. Kumar, S.K. Mehta, Semicond. Sci. Technol. 24 (9) (2009) 9.
[25] J. Kolodzey, E.A. Chowdhury, T.N. Adam, Q. Guohua, I. Rau, J.O. Olowolafe, J.S. Suehle, C. Yuan, IEEE Trans. Electron Devices 47 (1) (2000) 121.
[26] W.H. Ha, M.H. Choo, S. Im, J. Non-Cryst. Solids 303 (1) (2002) 78.
[27] C. Lin, J. Kang, D. Han, D. Tian, W. Wang, J. Zhang, M. Liu, X. Liu, R. Han, Microelectron. Eng. 66 (1–4) (2003) 830.
[28] H. Bartzsch, D. Glöß, B. Böcher, P. Frach, K. Goedicke, Surf. Coat. Technol. 174–175 (2003) 774.
[29] N.J. Ianno, H. Enshashy, R.O. Dillon, Surf. Coat. Technol. 155 (2–3) (2002) 130.
[30] A.G. Erlat, B.M. Henry, J.J. Ingram, D.B. Mountain, A. McGuigan, R.P. Howson, C.R.M. Grovenor, G.A.D. Briggs, Y. Tsukahara, Thin Solid Films 388 (1–2) (2001) 78.
[31] J. Borges, F. Vaz, L. Marques, Appl. Surf. Sci. 257 (5) (2010) 1478.
[32] J. Borges, E. Alves, F. Vaz, L. Marques, In: M.F. Costa (Ed.), International Conference on Applications of Optics and Photonics, 8001, Spie-Int Soc Optical Engineering, Braga, 2011, p. 80010F.
[33] S. Dreer, R. Krismer, P. Wilhartitz, Surf. Coat. Technol. 114 (1) (1999) 29.
[34] S. Dreer, R. Krismer, P. Wilhartitz, G. Friedbacher, Thin Solid Films 354 (1–2) (1999) 43.
[35] T.M. Hartnett, S.D. Bernstein, E.A. Maguire, R.W. Tustison, Infrared Phys. Technol. 39 (4) (1998) 203.
[36] A. Pallone, J. Demaree, J. Adams, Nucl. Instrum. Methods Phys. Res., Sect. B 219–220 (2004) 755.
[37] C. Normand, J. Eur. Ceram. Soc. 5/3 (1989) 143.
[38] J.J. Guo, K. Wang, T. Fujita, J.W. McCauley, J.P. Singh, M.W. Chen, Acta Mater. 59 (4) (2010) 1671.
[39] N. Martin, A. Besnard, F. Sthal, F. Vaz, C. Nouveau, Appl. Phys. Lett. 93 (6) (2008) 064102.
[40] G. Reiss, J. Vancea, H. Hoffmann, Phys. Rev. Lett. 56 (19) (1986) 2100.
[41] N.P. Barradas, C. Jeynes, R.P. Webb, Appl. Phys. Lett. 71 (2) (1997) 291.
[42] A. Ruhm, B.P. Toperverg, H. Dosch, Phys. Rev. B 60 (23) (1999) 16073.
[43] R.A. Weller, Rev. Sci. Instrum. 72 (9) (2001) 3580.
[44] L.J. Van Der Pauw, Philips Res. Rep. 13 (1) (1958) 1.
[45] L.J. Van Der Pauw, Philips Tech. Rev. 20 (8) (1958) 220.
[46] D. Depla, J. Haemers, R. De Gryse, Thin Solid Films 515/2 (2006) 468 (SPEC. ISS.).
[47] J.A. Thornton, J. Vac. Sci. Technol. 15 (2) (1978) 171.
[48] D. Depla, G. Buyle, J. Haemers, R. De Gryse, Surf. Coat. Technol. 200 (14–15) (2006) 4329.
[49] D. Depla, S. Mahieu, R. Gryse, In: Reactive Sputter Deposition, vol. 109, Springer, Berlin Heidelberg, 2008, p. 153.
[50] D. Depla, S. Heirwegh, S. Mahieu, J. Haemers, R. De Gryse, J. Appl. Phys. 101 (1) (2007) 013301.
[51] D. Depla, R. De Gryse, Plasma Sources Sci. Technol. 10 (4) (2001) 547.
[52] D. Depla, S. Mahieu, Reactive Sputter Deposition, Springer Series in Materials Science, vol. 109, 2008.
[53] N. Jacobson, J. Chem. Educ. 78 (6) (2001) 814.
[54] R.T. Downs, K.L. Bartelmehs, G.V. Gibbs, M.B. Boisen, Am. Miner. 78 (9–10) (1993) 1104.
[55] I. Petrov, P.B. Barna, L. Hultman, J.E. Greene, J. Vac. Sci. Technol., A 21/5 (2003) S117.
[56] V.A. Lubarda, Mech. Mater. 35 (1–2) (2003) 53.
[57] F. Vaz, L. Rebouta, P. Goudeau, J.P. Riviere, E. Schaffer, G. Kleer, M. Bodmann, Thin Solid Films 402 (1–2) (2002) 195.
[58] J. Wang, Y.-H. Yu, S.C. Lee, Y.-W. Chung, Surf. Coat. Technol. 146–147 (2001) 189.
[59] M.K. Sinha, S.K. Mukherjee, B. Pathak, R.K. Paul, P.K. Barhai, Thin Solid Films 515 (4) (2006) 1753.
[60] D.S. McLachlan, Phys. Rev. B 25 (4) (1982) 2285.
[61] D.R. Lide, Handbook of Chemistry and Physics, 72nd edition CRC Press, Boston, 1991.
[62] A. Kusy, J. Appl. Phys. 62 (4) (1987) 1324.
[63] G.E. Pike, C.H. Seager, J. Appl. Phys. 48 (12) (1977) 5152.